Article:
Bossanyi, D.G. orcid.org/0000-0002-8804-802X, Matthiesen, M., Wang, S. et al. (9 more authors) (2021) Emissive spin-0 triplet-pairs are a direct product of triplet–triplet annihilation in pentacene single crystals and anthradithiophene films. Nature Chemistry, 13 (2). pp. 163-171. ISSN 1755-4330

https://doi.org/10.1038/s41557-020-00593-y

Emissive spin-0 triplet-pairs are a direct product of triplet-triplet annihilation in pentacene single crystals and anthradithiophene films.

David G. Bossanyi[1,*], Maik Matthiesen[2], Shuangqing Wang[1], Joel A. Smith[1], Rachel C. Kilbride[1], James D. Shipp[3], Dimitri Chekulaev[3], Emma Holland[4], John E. Anthony[4], Jana Zaumseil[2], Andrew J. Musser[1,5], and Jenny Clark[1,*]

[1]Department of Physics and Astronomy, The University of Sheffield, Sheffield, UK
[2]Institute for Physical Chemistry, Heidelberg University, Heidelberg, Germany
[3]Department of Chemistry, The University of Sheffield, Sheffield, UK
[4]Department of Chemistry, University of Kentucky, Lexington, KY, USA
[5]Department of Chemistry and Chemical Biology, Cornell University, Ithaca, NY, USA

*dgbossanyi1@sheffield.ac.uk, jenny.clark@sheffield.ac.uk

Abstract. Singlet fission and triplet-triplet annihilation represent two highly promising ways of increasing the efficiency of photovoltaic devices. Both processes are believed to be mediated by a biexcitonic triplet-pair state, ^{1}(TT). Recently however, controversy has arisen over the role of ^{1}(TT) in triplet-triplet annihilation. Here we use intensity-dependent, low-temperature photoluminescence measurements, combined with kinetic modelling, to show that distinct ^{1}(TT) emission arises directly from triplet-triplet annihilation in high-quality pentacene single crystals and anthradithiophene (diF-TES-ADT) thin films. This work demonstrates that a real, emissive triplet-pair state acts as an intermediate in both singlet fission and triplet-triplet annihilation and that this is true for both endo- and exo-thermic singlet fission materials.

Introduction

Photon up- and down-conversion are two of the most promising strategies for pushing photovoltaic efficiencies beyond the Shockley-Queisser limit[1]. Achieving efficient spectral conversion nevertheless remains challenging. Triplet-triplet annihilation and singlet fission in molecular systems offer an enticing solution[2]. These processes involve conversion between high-energy singlet (spin-0) excitons and pairs of low-energy triplet (spin-1) excitons[3,4], thereby effectively turning a single high-energy photon into two low-energy excitations, or vice versa.

The conversion from singlet to triplets is widely accepted to proceed via a correlated triplet-pair state usually denoted ^{1}(TT) in a process described by $S_1 \rightarrow {}^1(TT) \rightarrow (T..T) \rightarrow T_1 + T_1$[5–7]. ^{1}(TT) is a biexciton state with overall spin-0 (singlet), yet its spin wavefunction can be approximated as a superposition of pairs of individual triplet excitons[8–11]. Spectral signatures of this state are widely debated in part because the main method used to study it, transient absorption spectroscopy, provides very similar signatures for ^{1}(TT), (T..T) and free triplets. Calculations[12–14] suggest that this is particularly true in the visible spectral region where most experiments are performed. In addition, paramagnetic resonance techniques[15–17] are blind to spin-zero states such as ^{1}(TT).

Instead, the simplest and most explicit probes of the ^{1}(TT) state are direct ground state absorption or photon emission. While many authors have assigned features from emission spectra to ^{1}(TT)[18–27], recent work by Dover et al.[28] calls these assignments into question. In particular, they argue that the redshifted spectral features are not direct intermediates to singlet fission, i.e. ^{1}(TT), but emission from trap states which instead hinder singlet fission, as previously reported[29–32]. This is important because a lack of spectral signature of ^{1}(TT) implicitly questions the existence of ^{1}(TT) as a real, bound intermediate state[18], yet the nature and behaviour of possible intermediates have critical implications for the design of efficient up- or down-converters.

Dover et al. pointed out that an intermediate to singlet fission must also be present in the reverse process, triplet-triplet annihilation. They showed that this was not the case in concentrated TIPS-tetracene solutions. Here we study high-quality pentacene single crystals and thin films of 2,8-difluoro-5,11-bis(triethylsilylethynyl)anthradithiophene (diF-TES-ADT) and observe clear ^{1}(TT) emission via triplet-triplet annihilation. This demonstrates conclusively that in the solid state, which is most relevant to device applications, ^{1}(TT) plays the role of a bound intermediate state in *both* singlet fission (SF) and triplet-triplet annihilation (TTA).

Results and discussion

In order to study ^{1}(TT) produced via SF or TTA, we focussed on two materials as model systems: diF-TES-ADT (diftes) and pentacene.

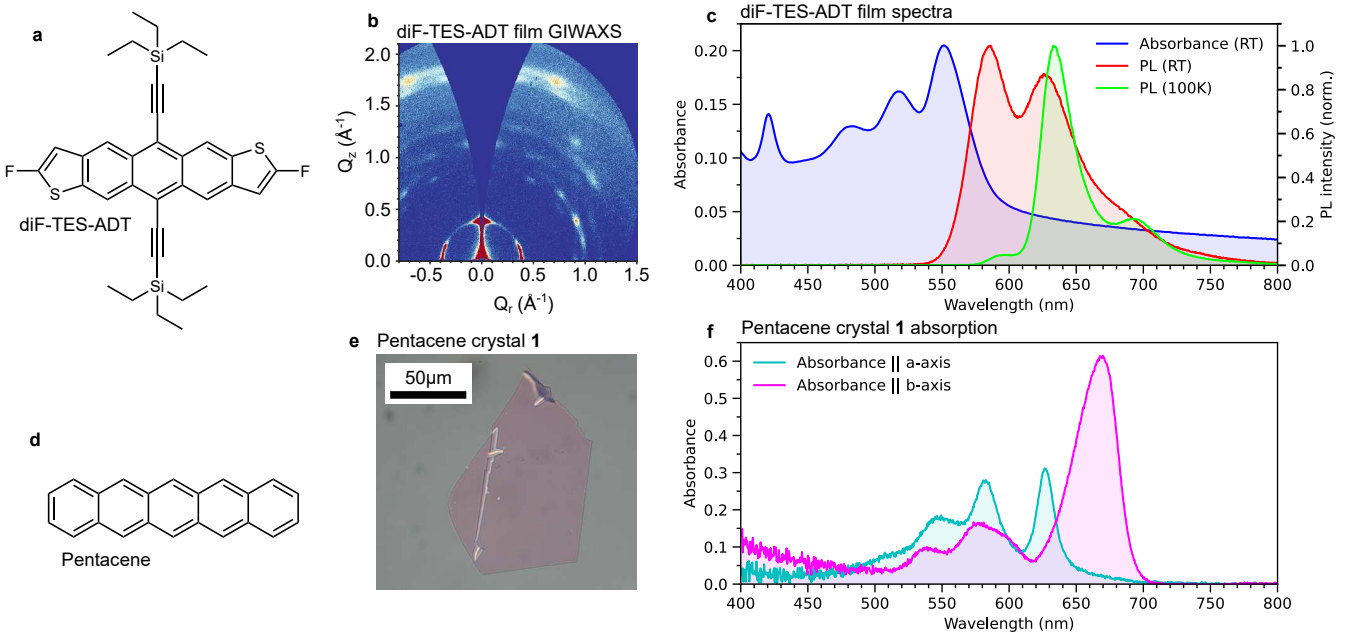

Figure 1 | Polycrystalline diftes thin films and single crystals of pentacene. **a**, Structure of the diF-TES-ADT (diftes) molecule. **b**, GIWAXS pattern of a diftes thin film indicating polycrystalline structure with primarily lamellar stacking. **c**, Absorption and temperature-dependent steady-state PL of a diftes thin film. At 100 K, the emission is primarily from ^{1}(TT) while at room temperature a significant contribution from S_1 is also present. **d**, Structure of the pentacene molecule. **e**, Bright-field microscope image of pentacene single crystal **1**. **f**, Polarised absorption spectra of pentacene single crystal **1** showing clear Davydov splitting of the 0-0 band.

We chose to focus on diftes (molecular structure in Fig. 1a) as our endothermic model system for several reasons. Firstly, compared with tetracene, it has a simple brickwork crystal structure[33], confirmed by our grazing incidence wide-angle X-ray scattering (GIWAXS) from a polycrystalline film in Fig. 1b (see also Supplementary Fig. 1). In addition there is no known polymorphism or other phase transition between 100 K and room temperature[18,34]. Secondly, we found diftes to be air- and photo-stable and were able to reliably make thin films with highly reproducible optical behaviour. Thirdly, distinct emission signatures have previously been attributed to ^{1}(TT)[18].

Fig. 1c shows the absorption and emission spectra of a diftes thin film. At room temperature the spectra arise from the vibronic progression of the $S_0 \leftrightarrow S_1$ transition. At low temperature however, the emission spectrum is dominated by a feature previously assigned to ^{1}(TT)[18]. We note that the ground state absorption spectrum does not change significantly with temperature (Supplementary Fig. 6).

We also chose to study pentacene (Fig. 1d) because of the energetic separation between S_1 and $2 \times T_1$[35], which ensures that annihilation of triplets cannot produce S_1[36]. Any signature of ^{1}(TT) due to TTA must therefore indicate that it is a real intermediate state. In addition, to minimise contributions from impurities and disorder, we grew high-quality optically thin single crystals (Fig. 1e). Pentacene crystallises in the herringbone arrangement[37], allowing us to compare results with those from brickwork diftes. Polarised ground state absorption measurements in Fig. 1f reveal strong Davydov splitting of the 0-0 transition, consistent with previous reports[38]. Full details of the crystal growth can be found in Section 1.2 of the Supplementary Information.

Bimolecular TTA populates ^{1}(TT) in diftes.

Time-resolved photoluminescence measurements of diftes thin films at 100 K in Fig. 2 reveal an instrument limited evolution from the S_1 fluorescence (red trace) to a redshifted, vibronically structured emission that persists, unchanged, for tens of microseconds. A previous study of diftes demonstrated that the delayed PL arises from the ^{1}(TT) state[18]. At first glance this assignment may seem surprising since the transition

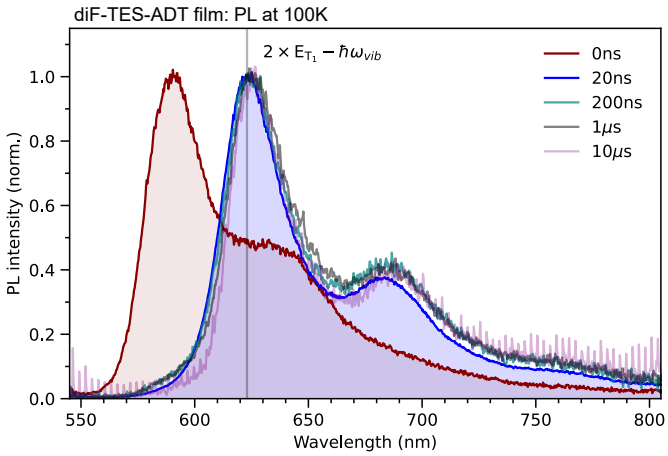

Figure 2 | Long-lived emissive ^{1}(TT) states in diftes thin films at 100 K. Time-gated emission spectra of a diftes thin film at 100 K. Immediately after excitation S_1 fluorescence is observed; structured ^{1}(TT) emission then persists, spectrally unchanged, for tens of microseconds. The highest energy band of the ^{1}(TT) emission coincides with twice the diftes triplet energy minus one vibrational quantum (0.17 eV), consistent with a Herzberg-Teller intensity borrowing mechanism[18].

dipole moment of ^{1}(TT) at its equilibrium nuclear geometry is zero due to the symmetry of its wavefunction. In fact, this is a zero-order approximation: ^{1}(TT) can couple to a symmetry-breaking vibrational mode, allowing it to mix with the nearby S_1 state. Since S_1 is a bright state, the transition dipole moment of ^{1}(TT) becomes non-zero to first order. This mechanism is known as Herzberg-Teller intensity borrowing[39] (or equivalently as the Albrecht B-term in Raman spectroscopy[40]). Since coupling to a vibration is required, the 0-0 peak of ^{1}(TT) emission is expected to be suppressed. Thus the luminescence spectrum of ^{1}(TT) is expected to form a vibronic progression, with the first visible peak (the 0-1 phonon replica) lying at approximately $2 \times E_{T_1} - \hbar\omega_{vib}$, i.e. twice the triplet energy minus one vibrational quantum[11,18,41]. In the case of diftes, twice the triplet energy of 1.08 eV[18] minus one vibrational quantum (0.17 eV) exactly matches the first peak of the delayed fluorescence (vertical line in Fig. 2), entirely consistent with Herzberg-Teller emission from the ^{1}(TT) state.

To determine whether ^{1}(TT) is formed from bimolecular TTA as well as through SF[18], we turn to the PL dynamics. Fig. 3 shows false-colour maps of time-resolved PL (TRPL) measured at three different excitation densities at 100 K (other temperatures 77–291 K in Supplementary Information Section 4). We extracted the S_1 and ^{1}(TT) spectral components using the Multivariate Curve Resolution Alternating Least Squares (MCR-ALS) algorithm[28,42] (full details in Section 4 of the Supplementary Information). The extracted spectra are shown to the right of the PL maps and the dynamics in the bottom panel.

The TRPL maps demonstrate an increase in relative emission intensity beyond 10 µs as the excitation density increases. On these timescales triplet excitons are the dominant excited states[18] and delayed emission can be reasonably attributed to bimolecular triplet-triplet annihilation (TTA)[43,44]. If TTA populates ^{1}(TT) by first forming S_1[28], we would expect to see a small S_1 contribution to the PL spectrum on these timescales. Importantly, we do not observe any such contribution, suggesting that the initial products of TTA are triplet-pair states rather than S_1 states (Supplementary Fig. 24). To confirm this, we examine the emission dynamics in more detail.

The excitation density dependent dynamics in Fig. 3d shows 3 distinct regions. During region I, the PL intensity decays exponentially with a single time constant of $\sim$ 25 ns (dashed red line). In region II, the decay becomes non-exponential but shows no dependence on excitation density. Region III marks the onset of the excitation density dependence, with higher densities leading to more intense emission.

This behaviour can be qualitatively explained as follows. During region I, emissive ^{1}(TT) states formed from sub-nanosecond SF (Supplementary Fig. 13) either decay to the ground state or form long-lived 'dark'

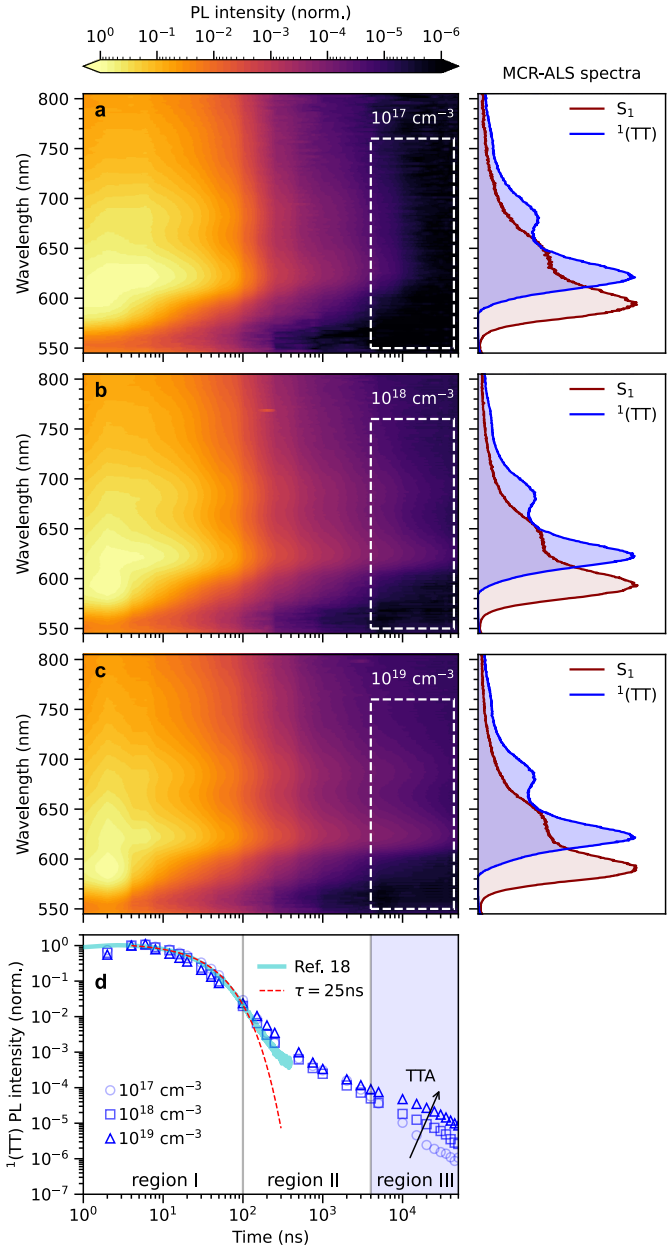

Figure 3 | ^{1}(TT) is the only emissive state formed from bimolecular TTA in diftes films at 100 K. **a-c**, False-colour maps of the TRPL measured at 100 K and normalised at 4 ns. Laser intensities corresponding to excitation densities of 10^{17}cm^{-3} (**a**), 10^{18}cm^{-3} (**b**) and 10^{19}cm^{-3} (**c**) were used. Dashed boxes highlight the regime of TTA, for which a relative increase in PL intensity is observed at higher excitation densities. No S_1 signatures are observed on these timescales. Spectral components extracted using MCR-ALS are shown to the right of each map. **d**, Excitation density dependent dynamics of the extracted ^{1}(TT) component (markers). Three regions are apparent: a mono-exponential decay with time constant ∼25 ns (region I) which has been previously measured (light-blue line)[18], followed by delayed emission in region II that becomes excitation density dependent (region III) after several microseconds. These three regions correspond to the initial decay of ^{1}(TT) (I), followed by geminate (T..T) recombination (II) and bimolecular TTA (III). Data corresponding to the light blue line in panel **d** obtained from Reference 18, licensed under a Creative Commons Attribution 4.0 International License.

triplets, as described previously[18] (light blue line, Fig. 3d). Region III shows the expected intensity dependence for bimolecular TTA. We assign the intermediate region II to geminate (T..T) recombination.

This qualitative description is backed up by kinetic modelling (Fig. 4). We find that we need to explicitly include two distinct triplet-pair populations in our rate model to reproduce our emission dynamics (Fig. 4a). This is only slightly different to the original Merrifield model[45]. We separate out the S_1 and ^{1}(TT) states (electronically coupled triplet-pairs) and take Merrifield's '(TT)' to be $(T..T)^l$ (weakly interacting triplet-pairs), see Fig. 4a. There are nine $(T..T)^l$ states ($l = 1, 2, ..., 9$) whose singlet character is given by the

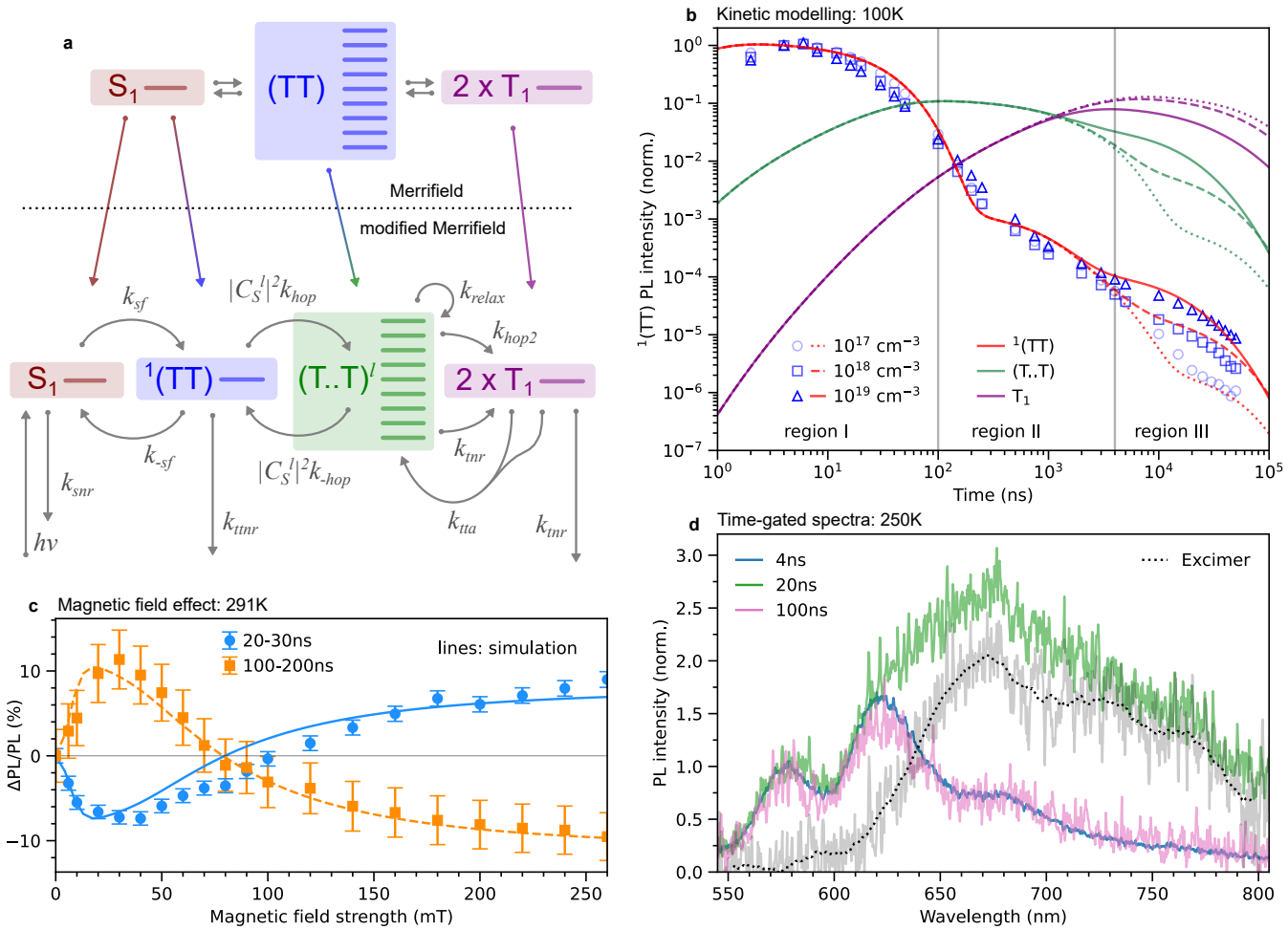

Figure 4 | The Merrifield kinetic scheme accurately captures the dependence of diftes PL on excitation density, temperature and magnetic field, provided that ^{1}(TT) is explicitly included. **a**, Our kinetic scheme (below dotted line) involves only a slight modification of the Merrifield model, with the explicit inclusion of the strongly exchange-coupled ^{1}(TT) state. **b**, Measured (blue markers) and simulated (red lines) ^{1}(TT) dynamics in diftes at 100 K normalised at 4 ns. The behaviour of (T..T) and T_1 are also shown. The scheme in panel **a** accurately captures the measured dynamics at all three excitation densities measured; this is replicated for five other temperatures (Supplementary Fig. S16). **c**, Measured (markers) and simulated (lines) effect of magnetic field on the room temperature PL of a single crystalline domain of diftes. Error bars were calculated from the small differences in measured PL intensity between spectra obtained while sweeping up in magnetic field and those obtained while sweeping back down. The differences arise principally from small fluctuations in laser intensity. The kinetic scheme from panel **a** reproduces all features of the measured effect at both time delays. **d**, Time-gated spectra of a diftes thin film at 250 K, 4, 20 and 100 ns after excitation with an initial excitation density of 10^{17}cm^{-3}. Excimer emission is clearly present at 20 ns in addition to contributions from S_1 and ^{1}(TT). Excimers are therefore distinct from ^{1}(TT) in diftes. The excimer spectrum (black line) was obtained by subtracting the normalised PL at 500 ns from that at 20 ns.

coefficients $|C_S^l|^2$ which give their degree of overlap with the singlet (see Supplementary Information Section 6.1).

This is equivalent to the currently accepted description of SF: $S_1 \leftrightarrow {}^1(TT) \leftrightarrow (T..T)^l \leftrightarrow T_1 + T_1$. We note that, as pointed out in a recent review[10], the nomenclature used in the literature can be confusing. Merrifield assumed that triplet-pairs have no electronic interaction (orbital overlap). In other words, the triplet-pair '(TT)' state described by Merrifield is identical to what we describe as (T..T). Others write ^{1}(TT) and implicitly include both the electronically coupled ^{1}(TT) and weakly-interacting (T..T)[18,46].

We use this scheme (Fig. 4a) to model our data with additional inclusion of spin-lattice relaxation[8] and non-radiative triplet decay from $(T..T)^l$ (i.e. $(T..T)^l \rightarrow T_1$). Both of these are found to have little effect. The governing rate equations are below and the resulting kinetics are shown in Fig. 4b.

$$\frac{d[\mathrm{S_1}]}{dt} = -(k_{sf} + k_{snr})[\mathrm{S_1}] + k_{-sf}[^1(\mathrm{TT})] \tag{1}$$

$$\frac{d[^1(\mathrm{TT})]}{dt} = k_{sf}[\mathrm{S_1}] - \left(k_{-sf} + k_{hop}\sum_{l=1}^{9}|C_S^l|^2 + k_{ttnr}\right)[^1(\mathrm{TT})] + k_{-hop}\sum_{l=1}^{9}|C_S^l|^2[(\mathrm{T..T})^l] \tag{2}$$

$$\begin{aligned}\frac{d[(\mathrm{T..T})^l]}{dt} &= k_{hop}|C_S^l|^2[^1(\mathrm{TT})] - \left(k_{-hop}|C_S^l|^2 + k_{hop2} + k_{tnr} + k_{relax}\right)[(\mathrm{T..T})^l] \\ &\quad + \frac{1}{8}k_{relax}\sum_{j\neq l}[(\mathrm{T..T})^j] + \frac{1}{9}k_{tta}[\mathrm{T_1}]^2\end{aligned} \tag{3}$$

$$\frac{d[\mathrm{T_1}]}{dt} = (k_{tnr} + 2k_{hop2})\sum_{l=1}^{9}[(\mathrm{T..T})^l] - 2k_{tta}[\mathrm{T_1}]^2 - k_{tnr}[\mathrm{T_1}] \tag{4}$$

In these equations square brackets denote concentrations of species in units of cm^{-3}. Rate constant definitions are shown in Fig. 4a. The $|C_S^l|^2$ coefficients are calculated from the spin Hamiltonian in Ref. 47, using zero-field splitting (D and E) parameters from Ref. 18 and molecular orientation calculated from the published crystal structure[33].

Fig. 4b shows the simulated ^{1}(TT) population dynamics, fitted globally to the measured excitation density-dependent ^{1}(TT) population. Where possible, rate constants were calculated or taken from transient absorption data (k_{sf}, k_{-sf}, k_{snr}). The remaining 7 were optimised to globally fit the full excitation density dependent dataset at each temperature and our uncertainty analysis (Supplementary Information Section 6.5) shows that they are tightly constrained. For full details of the kinetic modelling, see Methods and Supplementary Section 6. At every temperature, we find excellent agreement between simulation and data across all measured timescales and excitation densities (Supplementary Fig. 16).

Merrifield's model was originally developed to describe magnetic field-dependent fluorescence. Our kinetic scheme should, therefore, also be able to describe these effects, which arise as the $|C_S^l|^2$ coefficients vary with magnetic field according to the spin Hamiltonian[47]. Fig. 4c therefore shows a plot of ΔPL/PL as a function of magnetic field at two different delay times, measured at room temperature on a drop-cast sample (Supplementary Fig. 26, Methods, Supplementary Information Section 7). We then used our kinetic model to simulate the expected magnetic field dependence. The model (lines in Fig. 4c), reproduces the shape, magnitude and zero-crossing at both delay times.

We note that in our model, the magnetic field dependence arises specifically from ^{1}(TT) $\leftrightarrow$ (T..T), which occurs on longer timescales than ultrafast singlet fission ($\mathrm{S_1} \leftrightarrow {}^1$(TT)). Thus kinetic schemes that do not explicitly include both of these steps cannot correctly simulate the time dependence of the magnetic field effect, as demonstrated in Supplementary Fig. 30.

The kinetic scheme proposed by Dover et al.[28] includes an emissive excimer-like state that acts as a singlet trap rather than an intermediate to SF, but does not include any intermediates between $\mathrm{S_1}$ and $2 \times \mathrm{T_1}$. This model is not applicable here: the magnetic field-dependent PL requires the presence of ^{1}(TT) and (T..T) intermediates. Since ^{1}(TT) is a singlet state and thus expected to be emissive[11,18,41], we find no reason to assume that trap states are responsible for the emission we observe.

In fact, at a temperature of 250 K, we do observe distinct excimer-like emission *in addition to ^{1}(TT) and S_1 emission* (Fig. 4d). Whilst we do not wish to speculate further on the behaviour of the excimers, since we observe them only at this particular temperature and low excitation density, we reiterate that they are distinct from ^{1}(TT) in this system. This suggests that, while excimers may be present in singlet fission systems[28–32,48], they are not by themselves direct evidence of ^{1}(TT).

Having demonstrated that emissive triplet-pairs are populated through bimolecular TTA in a polycrystalline endothermic SF material, we now turn to our highly ordered, exothermic model system: single crystals

of pentacene. Previous reports of pentacene photoluminescence are scarce, and the spectral assignments[49,50] were made before the recent boom in singlet fission research. We therefore start by revisiting this literature and find evidence that the observed emission is consistent with ^{1}(TT). We further show, using fluence- and time-dependent measurements, that the ^{1}(TT) emission arises from bimolecular TTA.

Redshifted emission in pentacene single crystals arises from ^{1}(TT) rather than self-trapped excitons.

Fig. 5a shows delayed emission from single crystals of pentacene (micrographs in Fig. 5b). Despite the sub-100 fs, near-200% conversion of singlets to triplets in crystalline pentacene[35,51], we were able to measure weak photoluminescence from the crystals at 77 K. Just as for diftes, we found an instrument limited conversion from the S_1 fluorescence at around 690 nm to a redshifted feature that includes a peak at around 740 nm. Due to poor spectral sensitivity beyond around 820 nm (Supplementary Fig. 5), we cannot resolve the spectral shape at longer wavelengths and can only say that some emission is present in this region. This poor sensitivity, coupled with the weakness of the PL signal make the assignment of the redshifted feature considerably more challenging than for diftes.

We therefore begin by comparing our emission spectra to those previously measured[49,50,52] (Fig. 5c, Supplementary Fig. 33). The features that we observe are consistent with previously reported emission spectra of pentacene single crystals[49,50] and high-quality 20 nm thin layers[52], all of which report bands at around 1.85 eV, 1.65 eV, 1.5 eV and 1.35 eV. In Fig. 5c we plot the delayed emission measured in this work alongside that reported at 4 K and 100 K in Ref. 52 which we judge to be the least affected by artefacts, particularly self-absorption. A comparison with other reported spectra is presented in Fig. S33.

The three redshifted bands in the PL spectrum at 4 K (purple line in Fig. 5c) appear to form a vibronic progression. If all these bands arise from the same electronic state, the 0-1 and 0-2 peaks should follow a standard Franck-Condon progression whilst the 0-0 may be either enhanced or suppressed, depending on symmetry constraints[53]. We therefore fitted the two lowest energy peaks of the 4 K spectrum to the 0-2 and 0-1 bands of a Franck-Condon progression. We used the in-plane C-H bending mode at 1180 cm^{-1} as the main vibrational mode coupled to the electronic transition. Resonance Raman experiments have shown that this mode is resonant with both the S_1 fluorescence and the peak at 1.65 eV[54]. It also matches the separation between the 0-1 and 0-2 vibronic replicas in our polarised absorption measurement (Fig. 1f). Strikingly, the emission band at 1.65 eV coincides with the 0-0 peak of the resulting progression (dashed line in Fig. 5c), provided that its intensity is partially suppressed, as expected for emission enabled by Herzberg-Teller intensity borrowing. Within this context, intensity borrowing from S_1, which is expected to become superradiant below $\sim$ 10 K[11,38,55,56], may explain the observed temperature dependence of the 0-0 peak[49,52]. The 0-0 energy is slightly below that of two triplets in pentacene[57] (vertical line, Fig. 5c). The energy and spectral shape are therefore consistent with emission from ^{1}(TT).

Historically however, various alternative sources for the redshifted emission in pentacene have been proposed, namely defects[50] and self-trapped excitons[49,50,52]. It is also possible that excimers contribute to the redshifted emission. While difficult to rule out, we highlight that excimeric emission has been reported in several polyacenes and other SF materials[25,28–30,32,58], yet in every case the spectrum is broad, featureless and quite unlike the narrower, well resolved progression of peaks under consideration here.

Defects in single crystals may include extrinsic impurities or intrinsic vacancies or edge states. In the case of pentacene single crystals, extrinsic defects are reported to give rise to dominant emission at 1.5 eV[50], overlapping with the 0-1 vibronic feature described above. While we cannot rule out extrinsic defect emission in this spectral region, we expect it to be minimised in our crystals, grown using a two-stage sublimation of triple-sublimed starting material (see Methods). We focus instead on the 1.65 eV emission, which He et al.[50] demonstrated to be intrinsic. They showed resonant Raman enhancement of the 42 cm^{-1} phonon

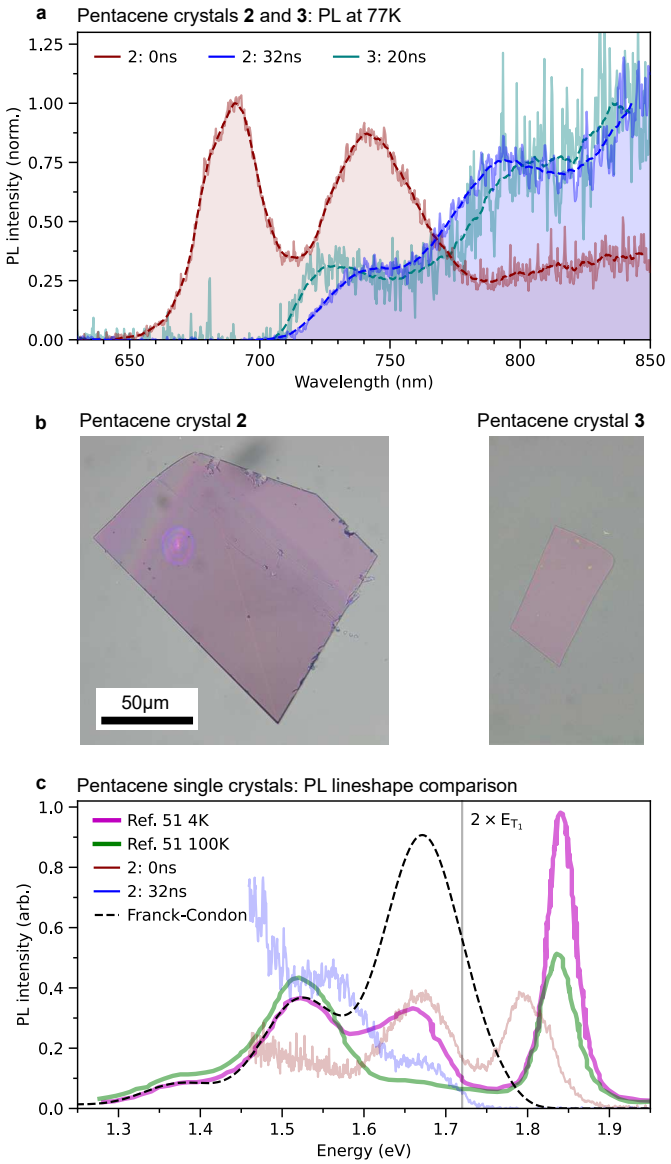

Figure 5 | Delayed emission from pentacene single crystals at 77 K is consistent with a Herzberg-Teller mechanism. a, Time-gated emission spectra of pentacene single crystals **2** and **3**; both the raw and smoothed spectra are shown. As for diftes, initial S_1 fluorescence is replaced by redshifted emission on longer timescales. **b**, Bright-field microscope images of pentacene single crystals **2** and **3**. **c** Delayed emission from **a** overlayed with luminescence spectra from Ref. 52. All the features in our time-resolved data are present in the previously measured spectra. The literature data is well described by a Franck-Condon progression (dashed black line) provided that the 0-0 band is suppressed. This type of emission is predicted for ^{1}(TT) states that emit via Herzberg-Teller intensity borrowing. Panel **c** adapted from Reference 52, with the permission of AIP Publishing.

mode across the 1.65 eV band at 8 K. This phonon mode is a sensitive indicator of intermolecular structure and is often used to distinguish between different polymorphs[59–61]. Such resonant enhancement of this pure mode suggests that the 1.65 eV emission arises from an intrinsic exciton species[50], rather than a vacancy or extrinsic impurity. Following previous literature[49], He et al. assigned it to a self-trapped exciton[50]. However, we argue in the following that self-trapped excitons are highly unlikely to be present in pentacene.

Exciton self-trapping occurs when low-energy intermolecular phonon modes, in other words lattice vibrations, act to localise the exciton wavefunction. The stability of self-trapped excitons in organic crystals is thus dependent on the exciton-lattice coupling.

The assignment of the 1.65 eV emission band in pentacene to self-trapped excitons[49] rests on a similar assignment in tetracene[62,63] and the lack of non-S_1 emission in anthracene[64,65]. To explain this trend, Matsui et al. extracted the exciton-lattice coupling for tetracene and anthracene from single exponential

fits to the temperature-dependent low-energy absorption edge[49,62–67] – the so-called Urbach tail[68]. This procedure can be problematic due to the large error in fitting a single exponential to the Urbach tail[69–72], for example in rubrene single crystals three exponentials are required[72]. However, the main issue with their analysis is the assumption that the excitons in anthracene and tetracene are 3D[62,65].

The dimensionality of the exciton is important because it determines the relationship between the slope extracted from Urbach tails and the exciton-lattice coupling, which in turn governs self-trapped exciton stability[73]. For a given slope, a 2D lattice gives weaker exciton-lattice coupling than a 3D one. In order to assign the non-S_1 emission in tetracene to self-trapped excitons, Matsui et al. were forced to invoke a 3D lattice, despite the evidence that excitons are 2D in tetracene[37,62,74]. Thus the *assumption* that self-trapped excitons are the source of the emission is built into their *assignment* (of the emission to self-trapped excitons), which we find to be a somewhat circular argument.

Taking the more physically realistic 2D lattice, self-trapped excitons should be unstable in both anthracene and tetracene[62], and the predicted trend in exciton-lattice coupling[75] would match widely accepted calculations of electron-lattice coupling by Brédas et al.[76,77]. Following this trend, exciton-lattice coupling should be even weaker in pentacene than in tetracene[76], although to our knowledge it has never been determined experimentally[78,79]. Such weak exciton-lattice coupling means that self-trapped excitons should be unstable in pentacene. There is therefore no clear basis for the assignment of redshifted emission in crystalline pentacene to self-trapped excitons[49,50,52].

Self-trapped excitons cannot explain the trend in non-S_1 emission in acenes: none in anthracene to redshifted in pentacene. The emission instead tracks the energy gap between S_1 and $2 \times T_1$[11]. Given this trend, together with the evidence that ^{1}(TT) is responsible for the non-S_1 emission in diftes[18], tetracene[19,20], TIPS-tetracene[24] and rubrene[18], as well as the spectral shape with suppressed 0-0 (Fig. 5c), we conclude that the 1.65 eV emission band in pentacene arises from ^{1}(TT).

Bimolecular TTA populates ^{1}(TT) in pentacene single crystals.

We demonstrated above that ^{1}(TT) is formed from bimolecular TTA in diftes. To see if this is also the case in exothermic pentacene, we investigate the behaviour of the ^{1}(TT) 1.65 eV emission band as a function of time and excitation density.

Fig. 6a,b shows previously reported room temperature transient absorption data of pentacene single crystals[36]. The data show the fluence dependence of the triplet photoinduced absorption (PIA) on ps (a) and ns (b) timescales. The authors of Ref. 36 showed that the triplet dynamics are governed by bimolecular TTA and they extracted the annihilation constant and triplet lifetime from a simple rate equation.

Ref. 36 was published before the role of ^{1}(TT) was well-established in pentacene. We therefore remodelled their data using a more complete description of the SF dynamics, in which $S_1 \rightarrow {}^1$(TT) occurs with a rate of $k_{sf} = 1/100\,\mathrm{fs}$[35,51] and ^{1}(TT) $\rightarrow T_1 + T_1$ occurs with a rate of $k_{sep} = 1/1\,\mathrm{ps}$[7,80,81]. The T_1 decay is governed by the rate constants established in Ref. 36. One of the conclusions of Ref. 36 is that not all triplet-triplet annihilation events in pentacene represent a loss of excited state population. Indeed we find here that a fraction of TTA events form ^{1}(TT) instead. The exact value of this fraction turned out to be unimportant and we take a value of 10% here. For the two-dimensional pentacene lattice, triplet excitons have infinite probability to collide[82], suggesting that both elastic and inelastic scattering events may be taking place. To reproduce the data in Fig. 6a,b, the only parameter we needed to vary was the conversion factor between the reported fluence values in units of $\mu\mathrm{J\,cm^{-2}}$ and excitation density in units of $\mathrm{cm^{-3}}$, since the necessary quantities were not reported in Ref. 36. The conversion factor used is further discussed in the Methods. Using no other free parameters, the modelled triplet dynamics match those of Ref. 36, as shown by the solid lines in Fig. 6a,b.

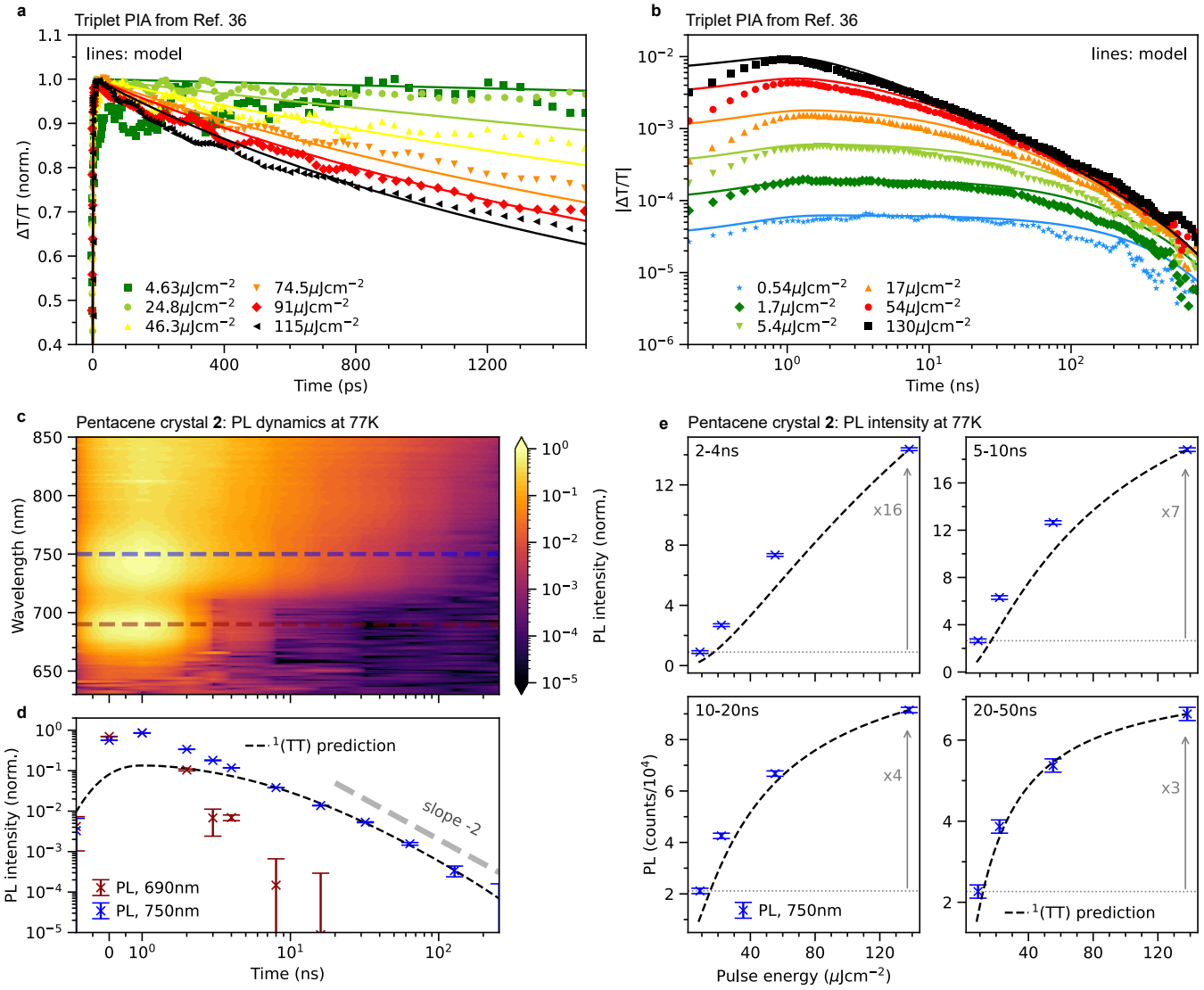

Figure 6 | Bimolecular TTA directly populates ^{1}(TT) states in pentacene single crystals. a,b Fluence-dependent photo-induced absorption (PIA) of triplets in a pentacene single crystal at room temperature (markers), reproduced from Ref. 36. The solid lines represent the bimolecular TTA model described in the text and methods. **c** False-colour map of the TRPL of pentacene single crystal **2**. Distinct bands at 690 nm (corresponding to S_1 emission) and 750 nm are observed. **d,e** The kinetics (**d**) and fluence dependence (**e**) of the 750 nm (1.65 eV) emission band (blue markers) match the behaviour of ^{1}(TT) predicted by the modelling of the data in **a,b** (dashed lines), demonstrating that this emission arises from bimolecular TTA. The error bars in **d,e** represent the standard deviation of the noise across a 10 nm spectral window around 750 nm. Panels **a** and **b** adapted with permission from Reference 36; copyright 2013 WILEY-VCH Verlag GmbH & Co. KGaA, Weinheim.

We next investigate whether the ^{1}(TT) behaviour predicted by this model is consistent with our measurements of the time and fluence dependence of the 1.65 eV emission band. Fig. 6c shows a false-colour map of the pentacene TRPL and the kinetics of the 1.65 eV (750 nm) band are plotted in Fig. 6d. On a timescale of tens of nanoseconds, the decay is a power law with a slope of -2. Fig. 6e shows the fluence dependence of the 1.65 eV emission at four different time delays. The intensity varies linearly with fluence within the first few nanoseconds and becomes increasingly sub-linear at later times. Both the power-law decay with a slope of -2, and the increasingly sub-linear intensity dependence are characteristic of bimolecular TTA[83–86].

The dashed lines of Fig. 6d,e show the *non-fitted*, normalised ^{1}(TT) behaviour predicted by the model used to describe the transient absorption data. All parameters, including the fluence scaling, remained the same as for Fig. 6a,b. The match to our time-gated fluence dependence is remarkable and as expected the slope of -2 in Fig. 6d is also reproduced. It is perhaps surprising that this independent model prediction and our data are so similar, given the difference in measurement temperature between Fig.s 6a,b and d,e

(the crystal dimensions and excitation source are comparable). For polycrystalline organic semiconductors, triplet transfer becomes slower at low temperature[81,87], as we observed for our diftes films. However, charge carrier mobility, and therefore expected triplet transfer rate[87], is independent of temperature for single crystal pentacene[88–90]. The room temperature model is therefore valid for our low-temperature PL data, and the excellent match confirms that ^{1}(TT) is populated directly through bimolecular TTA. S_1 cannot be involved in this process since it lies too high in energy.

We have shown that a weakly emissive ^{1}(TT) state is formed directly from bimolecular TTA in pentacene single crystals. Considerably brighter ^{1}(TT) emission is found in a range of acenes including diftes[18], tetracene[19,20], TIPS-tetracene[24] and rubrene[18]. The increase in ^{1}(TT) brightness between pentacene and diftes is explained by the reduced energy gap between ^{1}(TT) and S_1, which increases the Herzberg-Teller mixing. A consistent picture thus emerges of biexcitonic ^{1}(TT) intermediates that emit light through a Herzberg-Teller mechanism. Crucially for spectral upconversion, we have demonstrated here that such states are directly formed through bimolecular TTA.

Conclusions

We have shown here that ^{1}(TT) is an emissive, and real, intermediate state in both singlet fission and TTA, resolving a recent controversy in the literature. We find that ^{1}(TT) emission in our systems is distinct from excimer-like features. This work provides the first direct spectroscopic evidence that the strongly exchange-coupled ^{1}(TT) triplet-pair state can be directly formed from bimolecular triplet-triplet annihilation in both nominally endothermic and single crystal exothermic systems. In addition, we have shown that emission previously assigned to self-trapped excitons instead arises from ^{1}(TT).

Magnetic resonance techniques are blind to spin-zero states. Yet these states, including the strongly exchange-coupled ^{1}(TT), can be easily detected using photoluminescence spectroscopy. We find that we can track the population of ^{1}(TT) over the same timescales as transient electron paramagnetic resonance experiments[2,15]. This offers a missing piece to help unpick the spin physics of singlet fission and triplet-triplet annihilation.

In order to describe the emission dynamics and magnetic field effect, we used a modified Merrifield model which includes distinct (TT) and (T..T) populations. We find that to accurately describe our kinetic data, free triplets undergoing bimolecular TTA first recombine to form (T..T). (T..T) is rarely considered in studies of TTA up-conversion and yet its inclusion has profound implications for the overall efficiency. For example, the relative orientation of molecules and their magnetic dipole interactions influence the singlet character of the (T..T) states. It may therefore be possible to tune the system in such a way as to overcome the spin-statistical limit imposed by strongly exchange-coupled triplet-pairs[91,92].

References

[1] Day, J., Senthilarasu, S. & Mallick, T. K. Improving spectral modification for applications in solar cells: A review. *Renew. Energy* **132**, 186–205 (2019).

[2] Tayebjee, M. J. Y., McCamey, D. R. & Schmidt, T. W. Beyond Shockley–Queisser: Molecular approaches to high-efficiency photovoltaics. *J. Phys. Chem. Lett.* **6**, 2367–2378 (2015).

[3] Rao, A. & Friend, R. H. Harnessing singlet exciton fission to break the Shockley–Queisser limit. *Nat. Rev. Mater.* **2**, 17063 (2017).

[4] Frazer, L., Gallaher, J. K. & Schmidt, T. W. Optimizing the efficiency of solar photon upconversion. *ACS Energy Lett.* **2**, 1346–1354 (2017).

[5] Frankevich, E., Lesin, V. & Pristupa, A. Rate constants of singlet exciton fission in a tetracene crystal determined from the rydmr spectral linewidth. *Chem. Phys. Lett.* **58**, 127–131 (1978).

[6] Burdett, J. J. & Bardeen, C. J. Quantum beats in crystalline tetracene delayed fluorescence due to triplet pair coherences produced by direct singlet fission. *J. Am. Chem. Soc.* **134**, 8597–8607 (2012).

[7] Pensack, R. D. *et al.* Observation of two triplet-pair intermediates in singlet exciton fission. *J. Phys. Chem. Lett.* **7**, 2370–2375 (2016).

[8] Burdett, J. J., Piland, G. B. & Bardeen, C. J. Magnetic field effects and the role of spin states in singlet fission. *Chem. Phys. Lett.* **585**, 1–10 (2013).

[9] Scholes, G. D. Correlated pair states formed by singlet fission and exciton–exciton annihilation. *J. Phys. Chem. A* **119**, 12699–12705 (2015).

[10] Miyata, K., Conrad-Burton, F. S., Geyer, F. L. & Zhu, X.-Y. Triplet pair states in singlet fission. *Chem. Rev.* **119**, 4261–4292 (2019).

[11] Musser, A. J. & Clark, J. Triplet-pair states in organic semiconductors. *Annu. Rev. Phys. Chem.* **70**, 323–351 (2019).

[12] Khan, S. & Mazumdar, S. Theory of transient excited state absorptions in pentacene and derivatives: Triplet–triplet biexciton versus free triplets. *J. Phys. Chem. Lett.* **8**, 5943–5948 (2017).

[13] Khan, S. & Mazumdar, S. Optical probes of the quantum-entangled triplet-triplet state in a heteroacene dimer. *Phys. Rev. B* **98**, 165202 (2018).

[14] Khan, S. & Mazumdar, S. Free triplets versus bound triplet–triplet biexciton in intramolecular singlet fission materials: Structure–property correlations. *J. Phys. Chem. C* **124**, 1171–1177 (2020).

[15] Weiss, L. R. *et al.* Strongly exchange-coupled triplet pairs in an organic semiconductor. *Nat. Phys.* **13**, 176 (2016).

[16] Tayebjee, M. J. Y. *et al.* Quintet multiexciton dynamics in singlet fission. *Nat. Phys.* **13**, 182 (2016).

[17] Bayliss, S. L. *et al.* Geminate and nongeminate recombination of triplet excitons formed by singlet fission. *Phys. Rev. Lett.* **112**, 238701 (2014).

[18] Yong, C. K. *et al.* The entangled triplet pair state in acene and heteroacene materials. *Nat. Commun.* **8**, 15953 (2017).

[19] Burdett, J. J., Gosztola, D. & Bardeen, C. J. The dependence of singlet exciton relaxation on excitation density and temperature in polycrystalline tetracene thin films: Kinetic evidence for a dark intermediate state and implications for singlet fission. *J. Chem. Phys.* **135**, 214508 (2011).

[20] Tayebjee, M. J. Y., Clady, R. G. C. R. & Schmidt, T. W. The exciton dynamics in tetracene thin films. *Phys. Chem. Chem. Phys.* **15**, 14797–14805 (2013).

[21] Lukman, S. *et al.* Efficient singlet fission and triplet-pair emission in a family of zethrene diradicaloids. *J. Am. Chem. Soc.* **139**, 18376–18385 (2017).

[22] Hu, J. *et al.* New insights into the design of conjugated polymers for intramolecular singlet fission. *Nat. Commun.* **9**, 2999 (2018).

[23] Mauck, C. M. *et al.* Singlet fission via an excimer-like intermediate in 3,6-bis(thiophen-2-yl)diketopyrrolopyrrole derivatives. *J. Am. Chem. Soc.* **138**, 11749–11761 (2016).

[24] Stern, H. L. *et al.* Vibronically coherent ultrafast triplet-pair formation and subsequent thermally activated dissociation control efficient endothermic singlet fission. *Nat. Chem.* **9**, 1205 (2017).

[25] Stern, H. L. *et al.* Identification of a triplet pair intermediate in singlet exciton fission in solution. *Proc. Natl. Acad. Sci.* **112**, 7656–7661 (2015).

[26] Busby, E. *et al.* A design strategy for intramolecular singlet fission mediated by charge-transfer states in donor–acceptor organic materials. *Nat. Mater.* **14**, 426–433 (2015).

[27] Thampi, A. *et al.* Elucidation of excitation energy dependent correlated triplet pair formation pathways in an endothermic singlet fission system. *J. Am. Chem. Soc.* **140**, 4613–4622 (2018).

[28] Dover, C. B. *et al.* Endothermic singlet fission is hindered by excimer formation. *Nat. Chem.* **10**, 305–310 (2018).

[29] Schrauben, J. N., Ryerson, J. L., Michl, J. & Johnson, J. C. Mechanism of singlet fission in thin films of 1,3-diphenylisobenzofuran. *J. Am. Chem. Soc.* **136**, 7363–7373 (2014).

[30] Margulies, E. A. *et al.* Direct observation of a charge-transfer state preceding high-yield singlet fission in terrylenediimide thin films. *J. Am. Chem. Soc.* **139**, 663–671 (2017).

[31] Liu, H. *et al.* Synthesis and photophysical properties of a "face-to-face" stacked tetracene dimer. *Phys. Chem. Chem. Phys.* **17**, 6523–6531 (2015).

[32] Korovina, N. V. *et al.* Singlet fission in a covalently linked cofacial alkynyltetracene dimer. *J. Am. Chem. Soc.* **138**, 617–627 (2016).

[33] Subramanian, S. *et al.* Chromophore fluorination enhances crystallization and stability of soluble anthradithiophene semiconductors. *J. Am. Chem. Soc.* **130**, 2706–2707 (2008).

[34] Paudel, K., Giesbers, G., Van Schenck, J., Anthony, J. & Ostroverkhova, O. Molecular packing-dependent photoconductivity in functionalized anthradithiophene crystals. *Org. Electron.* **67**, 311–319 (2019).

[35] Wilson, M. W. B., Rao, A., Ehrler, B. & Friend, R. H. Singlet exciton fission in polycrystalline pentacene: From photophysics toward devices. *Acc. Chem. Res.* **46**, 1330–1338 (2013).

[36] Poletayev, A. D. *et al.* Triplet dynamics in pentacene crystals: Applications to fission-sensitized photovoltaics. *Adv. Mater.* **26**, 919–924 (2014).

[37] Campbell, R. B., Robertson, J. M. & Trotter, J. The crystal structure of hexacene, and a revision of the crystallographic data for tetracene and pentacene. *Acta Crystallogr.* **15**, 289–290 (1962).

[38] Hestand, N. J. *et al.* Polarized absorption in crystalline pentacene: Theory vs experiment. *J. Phys. Chem. C* **119**, 22137–22147 (2015).

[39] Orlandi, G. & Siebrand, W. Theory of vibronic intensity borrowing. comparison of Herzberg-Teller and Born-Oppenheimer coupling. *J. Chem. Phys.* **58**, 4513–4523 (1973).

[40] Albrecht, A. C. On the theory of Raman intensities. *J. Chem. Phys.* **34**, 1476–1484 (1961).

[41] Kim, H. & Zimmerman, P. M. Coupled double triplet state in singlet fission. *Phys. Chem. Chem. Phys.* **20**, 30083–30094 (2018).

[42] Jaumot, J., Gargallo, R., de Juan, A. & Tauler, R. A graphical user-friendly interface for MCR-ALS: a new tool for multivariate curve resolution in Matlab. *Chemom. Intell. Lab. Syst.* **76**, 101–110 (2005).

[43] Wallikewitz, B. H., Kabra, D., Gélinas, S. & Friend, R. H. Triplet dynamics in fluorescent polymer light-emitting diodes. *Phys. Rev. B* **85**, 045209 (2012).

[44] Akselrod, G. M. *et al.* Visualization of exciton transport in ordered and disordered molecular solids. *Nat. Commun.* **5**, ncomms4646 (2014).

[45] Johnson, R. C. & Merrifield, R. E. Effects of magnetic fields on the mutual annihilation of triplet excitons in anthracene crystals. *Phys. Rev. B* **1**, 896–902 (1970).

[46] Smith, M. B. & Michl, J. Recent advances in singlet fission. *Annu. Rev. Phys. Chem.* **64**, 361–386 (2013).

[47] Tapping, P. C. & Huang, D. M. Comment on "magnetic field effects on singlet fission and fluorescence decay dynamics in amorphous rubrene". *J. Phys. Chem. C* **120**, 25151–25157 (2016).

[48] Ye, C., Gray, V., Mårtensson, J. & Börjesson, K. Annihilation versus excimer formation by the triplet pair in triplet–triplet annihilation photon upconversion. *J. Am. Chem. Soc.* **141**, 9578–9584 (2019).

[49] Aoki-Matsumoto, T. *et al.* Excitonic photoluminescence in pentacene single crystal. *Int. J. Mod. Phys. B* **15**, 3753–3756 (2001).

[50] He, R., Chi, X., Pinczuk, A., Lang, D. V. & Ramirez, A. P. Extrinsic optical recombination in pentacene single crystals: Evidence of gap states. *Appl. Phys. Lett.* **87**, 211117 (2005).

[51] Wilson, M. W. B. *et al.* Ultrafast dynamics of exciton fission in polycrystalline pentacene. *J. Am. Chem. Soc.* **133**, 11830–11833 (2011).

[52] Anger, F. *et al.* Photoluminescence spectroscopy of pure pentacene, perfluoropentacene, and mixed thin films. *J. Chem. Phys.* **136**, 054701 (2012).

[53] Hestand, N. J. & Spano, F. C. Expanded theory of H- and J-molecular aggregates: The effects of vibronic coupling and intermolecular charge transfer. *Chem. Rev.* **118**, 7069–7163 (2018).

[54] He, R. *et al.* Resonant raman scattering in nanoscale pentacene films. *Appl. Phys. Lett.* **84**, 987–989 (2004).

[55] Lim, S.-H., Bjorklund, T. G., Spano, F. C. & Bardeen, C. J. Exciton delocalization and superradiance in tetracene thin films and nanoaggregates. *Phys. Rev. Lett.* **92**, 107402 (2004).

[56] Burdett, J. J., Müller, A. M., Gosztola, D. & Bardeen, C. J. Excited state dynamics in solid and monomeric tetracene: The roles of superradiance and exciton fission. *J. Chem. Phys.* **133**, 144506 (2010).

[57] Burgos, J., Pope, M., Swenberg, C. E. & Alfano, R. R. Heterofission in pentacene-doped tetracene single crystals. *Phys. status solidi* **83**, 249–256 (1977).

[58] Walker, B. J., Musser, A. J., Beljonne, D. & Friend, R. H. Singlet exciton fission in solution. *Nat. Chem.* **5**, 1019–1024 (2013).

[59] Della Valle, R. G. *et al.* Intramolecular and low-frequency intermolecular vibrations of pentacene polymorphs as a function of temperature. *J. Phys. Chem. B* **108**, 1822–1826 (2004).

[60] Della Valle, R. G. *et al.* Exploring the polymorphism of crystalline pentacene. *Org. Electron.* **5**, 1–6 (2004).

[61] Brillante, A. *et al.* Raman phonon spectra of pentacene polymorphs. *Chem. Phys. Lett.* **357**, 32–36 (2002).

[62] Mizuno, K., Matsui, A. & J. Sloan, G. Intermediate exciton-phonon coupling in tetracene. *J. Phys. Soc. Japan* **53**, 2799–2806 (1984).

[63] Nishimura, H., Yamaoka, T., Matsui, A., Mizuno, K. & J. Sloan, G. Exciton self-trapping in tetracene crystals: A case of shallow self-trap depth. *J. Phys. Soc. Japan* **54**, 1627–1633 (1985).

[64] Matsui, A. The polarized absorption edge and the davydov splitting of anthracene. *J. Phys. Soc. Japan* **21**, 2212–2222 (1966).

[65] Mizuno, K.-i. & Matsui, A. Frenkel exciton dynamics in anthracene under high pressure and quasi-free exciton state. *J. Phys. Soc. Japan* **55**, 2427–2435 (1986).

[66] Mizuno, K.-i., Matsui, A. & Sloan, G. J. Exciton-phonon interaction in tetracene single crystals under pressure. *Chem. Phys.* **131**, 423–433 (1989).

[67] Kobayashi, M., Mizuno, K.-i. & Matsui, A. High-pressure study of free excitons and self-trapped excitons in anthracene crystals at 1.5 k. *J. Phys. Soc. Japan* **58**, 809–812 (1989).

[68] Urbach, F. The long-wavelength edge of photographic sensitivity and of the electronic absorption of solids. *Phys. Rev.* **92**, 1324–1324 (1953).

[69] Coropceanu, V., Chen, X.-K., Wang, T., Zheng, Z. & Brédas, J.-L. Charge-transfer electronic states in organic solar cells. *Nat. Rev. Mater.* **4**, 689–707 (2019).

[70] Schweicher, G. *et al.* Molecular semiconductors for logic operations: Dead-end or bright future? *Adv. Mater.* **32**, 1905909 (2020).

[71] Raimondo, L., Silvestri, L., Borghesi, A. & Tavazzi, S. Exciton–lattice phonon coupling in organic semiconductor crystals beyond the static disorder. *J. Phys. Chem. C* **117**, 26248–26254 (2013).

[72] Salleo, A. Electronic traps in organic semiconductors. In *Org. Electron. Emerg. Concepts Technol.*, chap. 14, 341–380 (2013).

[73] Schreiber, M. & Toyozawa, Y. Numerical experiments on the absorption lineshape of the exciton under lattice vibrations. iii. the urbach rule. *J. Phys. Soc. Japan* **51**, 1544–1550 (1982).

[74] Turlet, J. & Philpott, M. R. Surface and bulk exciton transitions in the reflection spectrum of tetracene crystals. *J. Chem. Phys.* **62**, 4260–4265 (1975).

[75] Vukmirović, N., Bruder, C. & Stojanović, V. M. Electron-phonon coupling in crystalline organic semiconductors: Microscopic evidence for nonpolaronic charge carriers. *Phys. Rev. Lett.* **109**, 126407 (2012).

[76] Sánchez-Carrera, R. S., Paramonov, P., Day, G. M., Coropceanu, V. & Brédas, J.-L. Interaction of charge carriers with lattice vibrations in oligoacene crystals from naphthalene to pentacene. *J. Am. Chem. Soc.* **132**, 14437–14446 (2010).

[77] Coropceanu, V. *et al.* Hole- and electron-vibrational couplings in oligoacene crystals: Intramolecular contributions. *Phys. Rev. Lett.* **89**, 275503 (2002).

[78] Kurik, M. V. & Tsikora, L. I. Exciton–phonon interaction in crystals of linear polyacenes. *Phys. status solidi* **66**, 695–702 (1974).

[79] Klafter, J. & Jortner, J. Urbach rule in the optical spectra of crystalline and amorphous organic-solids. *Chem. Phys.* **26**, 421–430 (1977).

[80] Srimath Kandada, A. R., Petrozza, A. & Lanzani, G. Ultrafast dissociation of triplets in pentacene induced by an electric field. *Phys. Rev. B* **90**, 75310 (2014).

[81] Lee, T. S. *et al.* Triplet energy transfer governs the dissociation of the correlated triplet pair in exothermic singlet fission. *J. Phys. Chem. Lett.* **9**, 4087–4095 (2018).

[82] Suna, A. Kinematics of exciton-exciton annihilation in molecular crystals. *Phys. Rev. B* **1**, 1716–1739 (1970).

[83] Kepler, R. G., Caris, J. C., Avakian, P. & Abramson, E. Triplet excitons and delayed fluorescence in anthracene crystals. *Phys. Rev. Lett.* **10**, 400–402 (1963).

[84] Hall, J. L., Jennings, D. A. & McClintock, R. M. Study of anthracene fluorescence excited by the ruby giant-pulse laser. *Phys. Rev. Lett.* **11**, 364–366 (1963).

[85] Pope, M. & Swenberg, C. E. *Electronic Processes in Organic Crystals and Polymers.* Monographs on the physics and chemistry of materials (Oxford University Press, 1999).

[86] Ryasnyanskiy, A. & Biaggio, I. Triplet exciton dynamics in rubrene single crystals. *Phys. Rev. B* **84**, 193203 (2011).

[87] Köhler, A. & Bässler, H. What controls triplet exciton transfer in organic semiconductors? *J. Mater. Chem.* **21**, 4003–4011 (2011).

[88] Nelson, S. F., Lin, Y.-Y., Gundlach, D. J. & Jackson, T. N. Temperature-independent transport in high-mobility pentacene transistors. *Appl. Phys. Lett.* **72**, 1854–1856 (1998).

[89] Ostroverkhova, O. *et al.* Ultrafast carrier dynamics in pentacene, functionalized pentacene, tetracene, and rubrene single crystals. *Appl. Phys. Lett.* **88**, 162101 (2006).

[90] Minari, T., Nemoto, T. & Isoda, S. Temperature and electric-field dependence of the mobility of a single-grain pentacene field-effect transistor. *J. Appl. Phys.* **99**, 34506 (2006).

[91] Schulze, T. F. & Schmidt, T. W. Photochemical upconversion: present status and prospects for its application to solar energy conversion. *Energy Environ. Sci.* **8**, 103–125 (2015).

[92] Ieuji, R., Goushi, K. & Adachi, C. Triplet–triplet upconversion enhanced by spin–orbit coupling in organic light-emitting diodes. *Nat. Commun.* **10**, 5283 (2019).

Acknowledgements

D.G.B. and J.A.S. thank the EPSRC Centre for Doctoral Training in New and Sustainable Photovoltaics (EP/L01551X/1) for studentship support. J.Z. and M.M. acknowledge funding by the Deutsche Forschungsgemeinschaft via the Collaborative Research Center 'N-Heteropolycycles as Functional Materials' (SFB 1249, C06). J.D.S. thanks the Grantham Centre for Sustainable Futures for studentship support. J.E.A. and E.H. thank the US NSF (CHE-1609974) for support of material synthesis. We thank EPSRC for a Capital Equipment award, which provided the Lord Porter Laser Laboratory Facility used in this study. We further thank Xenocs for their ongoing support through the X-ray scattering user program at the University of Sheffield and we thank the EPSRC for funding the purchase of this instrument. We thank Rahul Jayaprakash for assistance with the polarised absorption measurement. Finally, we would like to thank Philippe Green and Mark Wilson from the University of Toronto for providing us with inorganic semiconductor nanocrystals for triplet sensitisation.

Correspondence and requests for materials should be addressed to J.C.

Author contributions

J.C. conceived the project. D.G.B., A.J.M. and J.C. designed the experiments. D.G.B. made the diF-TES-ADT samples and performed all of the spectroscopic measurements, data analysis and kinetic modelling. S.W. performed the magnetic field dependent measurement. M.M. fabricated and characterised the pentacene single crystals under the supervision of J.Z. J.A.S. and R.C.K. performed the GIWAXS and AFM measurements. J.D.S. and D.C. assisted with transient absorption measurements. E.H. and J.E.A. provided the diF-TES-ADT. D.G.B. and J.C. wrote the manuscript with input from A.J.M.

Competing interests

The authors declare no competing interests.

Methods

diftes thin film preparation

diF-TES-ADT (diftes) was synthesised following previously reported procedures[33] and dissolved in anhydrous toluene at a concentration of $15\,\mathrm{mg\,ml^{-1}}$. Thin films were prepared by spin-coating from solution onto pre-cleaned quartz-coated glass at a speed of 1200 rpm for 40 s. Film thickness was measured to be $\sim 60\,\mathrm{nm}$ using stylus profilometry (Dektak, Bruker). All thin film preparation was carried out in a nitrogen-filled glovebox.

Samples for TRPL measurements were not encapsulated since the measurement took place in an inert helium atmosphere. In general, exposure to light and air was kept to a minimum and all samples were stored in a nitrogen-filled glovebox. For transient absorption and magnetic field effect measurements, the sample was encapsulated inside the glovebox using a thin glass coverslip and a 2-component epoxy resin (Araldite).

Morphological characterisation of diftes thin films

Grazing incidence wide-angle X-ray scattering (GIWAXS) measurements were taken using a Xenocs Xeuss 2.0 system with a liquid Ga MetalJet X-ray source (Excillum). The 9.243 keV X-ray beam was collimated with two sets of slits and the sample chamber, flight tube and detector were held under vacuum to minimise

additional scatter. Scattered X-rays from the sample surface were collected with a Pilatus3R 1M hybrid photon counting detector (Dectris) at a distance of 330 mm and a grazing incidence angle of 0.18°. Geometry was refined with a AgBe calibrant after which azimuthal integrations of the data were performed with a full pixel-splitting algorithm to account for issues with detector resolution and binning at small angles[93]. The 2D data was corrected and processed with the GIXSGUI MATLAB toolbox[94]. Powder XRD patterns and crystal packing images for diftes were simulated in Mercury, using previously reported crystallographic information files[33,95]. Analysis of the processed GIWAXS data is presented in Supplementary Fig. 1b.

Atomic force microscopy (AFM) measurements were performed in tapping mode using a scanning force microscope (Veeco Dimension 3100) with a nanoscope 3 A feedback controller. The AFM tips were TESPA-V2 probes (Bruker) with a resonance of around 320 kHz and spring constant of 42 $\mathrm{N\,m^{-1}}$. Gwyddion 2.54 software was used to process the AFM images (levelling by mean plane subtraction, row alignment, horizontal scar correction, zero correction for the height scale). An AFM image of one of the diftes films is shown in Supplementary Fig. 1c.

Pentacene single crystal growth

Pentacene (≥99.995%, triple-sublimed grade) was purchased from Merck. Single crystals were grown by physical vapour transport[96,97] (PVT). A horizontal PVT furnace (Trans Temp, Thermcraft) was used for the growth, and the apparatus was enclosed to prevent possible photo-degradation.

First sublimation Quartz tubes used inside the PVT furnace were first cleaned with soap and a succession of solvents before being baked at 325 °C for 16 h and allowed to cool fully. 79 mg of starting material was placed at the end of the furnace and the whole assembly was purged under flowing ultra high purity argon gas (99.999%, 50 $\mathrm{cm^3\,min^{-1}}$) for 21 h. This gas flow was then maintained for the entirety of the first sublimation. The temperature of the starting material was next raised to 137 °C for 2.5 h and finally set at 289 °C and left for 3 d before being allowed to cool to room temperature. During the first sublimation, pentacene crystals were observed in the hottest part of the crystallization zone ∼220–260 °C, with orange, green and yellow impurities forming in the cooler parts as shown in Supplementary Fig. 2.

Second sublimation The purple pentacene crystals grown in the first sublimation were used as the starting material for the second sublimation. The remaining quartz tubes were cleaned and baked as before, and again the whole assembly was purged with argon for 17 h, this time at a flow rate of 30 $\mathrm{cm^3\,min^{-1}}$). The temperature was next held at 137 °C for 2 h, then set to 289 °C for sublimation. After 1 d of sublimation, pentacene crystals were observed in the crystallization zone within a temperature range of ∼220–260 °C. No impurities were observed during the second sublimation.

Pentacene single crystal characterisation Following the second sublimation, pentacene single crystals were selected and laminated onto pre-cleaned quartz-coated glass. Bright-field, dark-field and cross-polarised images were recorded using a white-light microscope (Olympus BX51) and are shown in Supplementary Fig. 3a-i. No image processing was used for the micrographs. Crystal thickness was measured by taking a step profile using AFM (Dimension Icon, Bruker fitted with Scanasyst-Air tips); these results are displayed in Supplementary Fig. 3k-l.

Supplementary Fig. 4 shows a surface scan of crystal **2**, recorded using the same AFM instrument as for the thickness measurements. Terraces with an average step height of 1.6 nm were found, corresponding to the c-axis of the pentacene crystal[37] and confirming that, as expected[38], the platelet-shaped crystals grew in the a-b plane.

The polarised absorption measurement reported in the main text was performed on crystal **1**, since this was the largest but thinnest of the crystals. Time-resolved PL measurements were performed on crystals **2** and **3**, these being the largest and most perfect respectively.

The crystals were not encapsulated, but exposure to air and light was kept to a minimum and the crystals were stored in a nitrogen-filled glovebox.

Steady-state absorption and PL measurements

Room temperature ground state absorption of thin film samples was performed using a UV-visible spectrophotometer (Cary60, Agilent). For temperature-dependent absorption and PL, the sample was mounted in a closed-cycle helium cryostat (OptistatDry BLV, Oxford Instruments). White light for absorption measurements was provided by a deuterium-halogen lamp (DH2000-BAL, Ocean Optics) and excitation for PL measurements was provided by a 405 nm CW laser diode (Thorlabs). Spectra were recorded using a fibre-coupled spectrometer (HR2000+ES, Ocean Optics). A 435 nm longpass filter (GG435, Schott) was placed before the detector for PL measurements.

The polarised absorption of the pentacene single crystals was measured by focussing light from a tungsten lamp through a variable linear polariser and onto the crystal using a 100 mm focal length lens. Transmitted light was collected with a 50× Mitutoyo Plan Apo SL infinity-corrected objective and delivered to a spectrometer (Andor).

Time-resolved PL measurements

For time-resolved measurements, samples were situated in the helium exchange gas of a nitrogen bath cryostat (Optistat DN, Oxford Instruments). The temperature of the exchange gas was controlled using an inbuilt heater and thermocouple connected to an external PID controller (Mercury iTC, Oxford Instruments). The sample temperature was assumed to have stabilised at that of the exchange gas once repeated fluorescence measurements yielded exactly the same spectrum and intensity. Excitation was provided by the frequency-doubled output of a Q-switched Nd:YVO4 laser (Picolo-AOT, Innolas). The laser produces pulses at 5 kHz with temporal width < 500 ps and a wavelength of 532 nm. The photoluminescence was detected by a spectrograph (Shamrock 303i, Andor) and time-gated intensified CCD (iStar DH334T-18U-73, Andor). The grating used in the spectrometer is blazed at 500 nm and has a groove density of 150 lines per mm. The image intensifier employs a gen. 3 VIH photocathode. The photocathode and grating largely determine the spectral sensitivity of the detector, which was measured using a calibrated light source and is plotted in Supplementary Fig. 5. The intensified CCD (iCCD) was cooled to $-30\,^{\circ}$C by a Peltier element during measurements. A combination of a 532 nm notch filter and 550 nm longpass filter (OG550, Schott) were used to cut out pump scatter.

The iCCD allows PL spectra to be collected (integrated) during a specified gate width. The gate opens at a specified gate delay after the laser pulse, remains open for the specified gate width during which photons are collected and then closes. This cycle is typically repeated over hundreds of laser shots for each data point and the result accumulated. This mode of operation allows for the recording of time-gated PL spectra.

In order to measure PL kinetics, the gate delay is incremented by a gate step for each data point. However, since the PL signal decreases with time, the signal to noise ratio gets progressively worse with time. To overcome this and take advantage of the excellent sensitivity of the detector over the full range of timescales that we can measure, we record the PL kinetics in short sections, using a constant gate step and gate width for each section. The gate width is always less than or equal to the gate step. As we move further from time zero, the gate width and step used for each section are increased (gain and exposure may be increased as well). We are careful to include a temporal overlap between the end of the preceding section

and the start of the following one. Backgrounds are also collected for each section.

Data processing first involves subtracting the background from every spectrum in each section. Next, at each point of overlap between sections, the second section is scaled by a constant factor until the spectra at the overlapping time exactly match in shape and intensity. In this way, the true PL kinetics can be obtained over many orders of magnitude in time and intensity whilst maintaining a good signal to noise ratio. We note that the scaling procedure means that plotting the y-axis in absolute units (such as counts) would not give a true indication of the fidelity of the data, since the counts are scaled differently for each section. Instead the fidelity of the data should be examined by (a) looking at the raw spectra by eye and/or (b) looking at the error bars, which are given as the standard deviation of the noise across the spectral range for which the data point was averaged (±5 nm in all the data presented in this way here.)

Typical values for intensifier gain and exposure time are as follows. diftes: gain of around 2000 or lower, exposure time around 1 s or lower. Pentacene: gain of around 3000-4000, exposure time 5–10 s.

Spectra presented in the main text have been corrected for the spectral sensitivity of our iCCD and for filter transmission. The spectral sensitivity of our iCCD is shown in Supplementary Fig. 5.

Measurements of average laser power P were carefully converted into values of average exciton density N using the following expression:

$$N = F_A\,(1 - F_S)\,R_P \frac{P}{f \pi r_x r_y d} \frac{\lambda}{hc} \tag{5}$$

Here, F_S and F_A represent the fraction of incident light scattered and absorbed by the sample respectively, evaluated from the UV-visible transmission spectrum (0.44 and 0.18 respectively for diftes), R_P is the ratio of measured power between the sample position and power meter position (0.58 for our setup), f is the repetition rate of the laser (1 kHz for internally triggered power measurements), r_x and r_y are the radii of the excitation beam spot, measured as 130 nm and 100 nm respectively with a CCD beam profiler (Thorlabs), d is the sample thickness, λ is the excitation wavelength and h and c are Planck's constant and the speed of light respectively.

Transient absorption spectroscopy

A Ti:sapphire regenerative amplifier (Spitfire ACE PA-40, Spectra-Physics) providing 800 nm pulses (40 fs FWHM, 10 kHz, 1.2 mJ) was used to generate both the pump and probe beams. Tuneable narrowband pump pulses at 532 nm were generated in an optical parametric amplifier (TOPAS Prime, Light Conversion). Probe pulses spanning the ranges 350–700 nm and 850–1300 nm were generated by focussing a portion of the 800 nm beam through a continuously translating calcium fluoride or sapphire crystal, respectively. Pump-probe delay was controlled using a motorized linear stage. Detection was carried out using a commercial instrument (Helios, Ultrafast Systems) equipped with CMOS and InGaAs detectors for the UV-visible and NIR probe regions respectively. The pump and probe polarizations were set to magic angle. Pump beam spot size was measured at the sample position using a CCD beam profiler (Thorlabs).

Multivariate curve resolution alternating least squares

Spectral components and their dynamics were extracted from the diftes TRPL data at each excitation density and temperature using Multivariate Curve Resolution Alternating Least Squares (MCR-ALS)[42]. Two components only were used in each case and pure spectra were used as the initial point. Both the spectra and concentrations were forced to be non-negative using fast non-negative least squares. The spectral matrix was normalised and the algorithm run until convergence was achieved.

Kinetic modelling for diftes

Algorithms All simulations and fitting were performed using custom-made python code. The systems of rate equations were solved using the LSODA algorithm from MINPACK as implemented in SciPy's `odeint`. The Levenberg-Marquardt algorithm from MINPACK as implemented in SciPy's `least_squares` was used to globally fit the kinetic models to the exciton density-dependent data through variation of certain rate constants. The logarithm of data and simulation were taken when calculating residuals in order to treat all timescales equally. Rate constants were manually adjusted prior to fitting to ensure convergence to the global minimum.

Spin Hamiltonian Spin wavefunction overlap factors $|C_S^l|^2$ were computed using custom-made python code following the method laid out by Tapping and Huang[47]. The calculation requires knowledge of the relative orientation of adjacent molecules: this was determined from the published crystal structure of diftes[33]. The zero-field splitting parameters D and E are also needed. For diftes we took values derived from PL quantum beating ($D = 1 \times 10^{-6}$eV, $E = 3 \times 10^{-6}$eV)[18]. The strength of the triplet-triplet dipole-dipole interaction was taken as 60 neV[17].

Instrument response We took the instrument response of our iCCD into account in a somewhat crude fashion by assuming an exponentially rising population of photoexcited singlet excitons. Mathematically, this involved introducing an additional rate equation to the kinetic models for the pre-excitation ground state as follows:

$$\frac{d[\mathrm{GS}]}{dt} = -k_{gen}[\mathrm{GS}] \tag{6}$$

$$\frac{d[\mathrm{S_1}]}{dt} = k_{gen}[\mathrm{GS}] + ... \tag{7}$$

We calculated the initial value of [GS] according to equation 5. We then determined the value of k_{gen} by modelling the decay of the S_1 state in pentacene single crystal **2**. Since singlet fission is known to occur within 100 fs in pentacene[51], the PL decay of S_1 is instrument-limited. We found a value of 1.8 ns^{-1} using this method and used it in all further modelling. We note that this is a reasonable number, given the laser pulse width of < 500 ps. The precise shape of the instrument response function (IRF) is immaterial since all the dynamics of interest occur on longer timescales. The decay of the pentacene S_1 fluorescence (Figure 6d in the main text) gives a very reasonable idea of the IRF, since the decay constant is known to be ≤ 100 fs[51]. This is equivalent to (for example) measuring the decay of pump scatter.

Fixed rate constants We determined the value of the singlet fission rate constant k_{sf} from TA measurements as 10 ns^{-1} (Supplementary Fig. 13). Since this rate is thought to be independent of temperature[98], we fixed it for all the modelling presented here.

We set the rate constant for conversion of ^{1}(TT) back to S_1 (k_{-sf}) to zero for temperatures of 100 K and below since little or no singlet contribution was observed in the delayed luminescence. From 150 K upwards, we estimated the rate using the following relation, which assumes a thermal equilibrium between ^{1}(TT) and S_1:

$$\frac{k_{-sf}}{k_{sf}} = \frac{\mathrm{P}_S}{\mathrm{P}_{TT}} \frac{k_{ttr}}{k_{sr}} \tag{8}$$

Here $\mathrm{P}_S/\mathrm{P}_{TT}$ is the ratio of S_1 PL to ^{1}(TT) PL in the delayed luminescence and we took the ratio of radiative rates k_{ttr}/k_{sr} to be 1/40 as previously reported[18].

Finally, we took the intrinsic lifetime of the singlet to be 12 ns, as measured using TA for dilute solutions of diftes (Supplementary Fig. 13). We note however, that the precise values of all these rate constants have a negligible effect on the ^{1}(TT) population dynamics (Supplementary Information Section 6.5).

Preparation of a diftes crystal for measurement of magnetic field effects

diftes was dissolved at a concentration of 5 mg mL^{-1} in toluene. A pre-cleaned quartz-coated glass substrate was placed in a small petri dish situated inside a larger petri dish containing 1 mL of toluene. 80 µL of the diftes solution was drop-cast quickly onto the substrate and the whole system covered with another glass dish. The solvent was allowed to slowly evaporate overnight. This procedure yielded large single crystalline domains many hundreds of microns in size (Supplementary Fig. 26). The sample was made and encapsulated in a nitrogen-filled glovebox. Encapsulation was done using Araldite epoxy resin and a glass coverslip. The micrograph (Supplementary Fig. 26) was collected using a Nikon Eclipse ME600 microscope in reflection mode with crossed polarisers. No image processing was used.

Magnetic field effect measurements

The sample was placed between the poles of an electromagnet. The measurement was performed at room temperature, since the pole separation required for low temperature measurements was much too great to achieve the required magnetic field strengths. Excitation was provided by the frequency-doubled output of a Q-switched Nd:YVO4 laser (Picolo-AOT, Innolas). The laser produces pulses at 5 kHz with temporal width < 500 ps and a wavelength of 532 nm. The photoluminescence was collected and sent via optical fibre to a spectrograph (Shamrock 303i, Andor) and time-gated intensified CCD (iStar DH334T, Andor) for detection. Magnetic field strength was measured using a gauss meter. A spot size of 50 µm was evaluated by translating a razor blade through the focal point. Magnetic field strength was measured using a Gauss meter.

The PL dynamics at 0 mT were measured first in order to check rate constant values for magnetic field effect modelling (see below). The effects of magnetic field on PL were measured by recording PL spectra at a series of magnetic field strengths at two different gate delays: 20–30 ns and 100–200 ns. The measured spectra were identical in shape and magnitude both while sweeping upwards and subsequently downwards in magnetic field strength (Supplementary Fig. 27), allowing us to rule out any effects from photo-degradation or laser power fluctuations and giving us high confidence in the reproducibility of the observed magnetic field effect. Spectra were integrated along the wavelength axis and the magnetic field effect evaluated as

$$\frac{\Delta PL}{PL}(B) = \frac{PL(B) - PL(0)}{PL(0)} \tag{9}$$

Simulation of the measured magnetic field effect

The magnetic field effect was simulated using the kinetic scheme outlined in the main text and Fig. 4a. The rate constants were varied slightly from the values used for the thin film and the zero field splitting parameters D and E were adjusted within their reported experimental errors[18]. This procedure is described in detail in Supplementary Information Section 7.

Kinetic modelling for pentacene

In Ref. 36 the triplet photoinduced absorption (PIA) was measured as a function of pulse energy and fitted to a simple bimolecular annihilation model given by:

$$\frac{d[\mathrm{T_1}]}{dt} = -k_{tta}[\mathrm{T_1}]^2 - k_{tnr}[\mathrm{T_1}] \tag{10}$$

Where $k_{tta} = 1.2 \times 10^{-10}\,\mathrm{cm^3\,s^{-1}}$ and $k_{tnr} = 1/500\,\mathrm{ns}$. Here we simply extended this model to include the full singlet fission process, as described in the main text. The rate equations are given by:

$$\frac{d[\mathrm{S_1}]}{dt} = -\left(k_{sf} + k_{snr}\right)[\mathrm{S_1}] \tag{11}$$

$$\frac{d[^1(\mathrm{TT})]}{dt} = k_{sf}[\mathrm{S_1}] - k_{sep}[^1(\mathrm{TT})] + f k_{tta}[\mathrm{T_1}]^2 \tag{12}$$

$$\frac{d[\mathrm{T_1}]}{dt} = 2k_{sep}[^1(\mathrm{TT})] - 2k_{tta}[\mathrm{T_1}]^2 - k_{tnr}[\mathrm{T_1}] \tag{13}$$

Here f is the fraction of TTA events that form ^{1}(TT). We found the precise value to be unimportant, so long as it is less than unity. We used a value of 10%. We note that in Ref. 36, one of the conclusions was that not all triplet-triplet annihilation caused a loss of excited states in pentacene. Our data suggests that this is because a fraction of TTA events in fact form ^{1}(TT). The rate equations were solved using similar python code to that described above for diftes. Finally, the populations were convolved with a Gaussian IRF to mimic the instrument response of the different TA and PL setups. We take the triplet PIA to be proportional to $[^1(\mathrm{TT})] + [\mathrm{T_1}]$.

In order to apply this model to the experimental data, the measured laser pulse energies (units of $\mu\mathrm{J\,cm^{-2}}$) had to be converted to units of $\mathrm{cm^{-3}}$. Ref. 36 did not report their calculation for this conversion. We therefore obtained a constant conversion factor simply by applying the model to their fluence-dependent TA data and varying its value until the data was well reproduced by eye and the simulation matched that reported in Ref. 36. The value obtained was $8 \times 10^{15}\,\mathrm{cm^{-1}\,\mu J^{-1}}$. Taking a typical crystal thickness of around 300 nm[36], this number implies that roughly 10% of photons in each pulse result in an excitation in the crystal. This seems reasonable since (a) the crystals in our measurement (and those in Ref. 36) are of a size similar to our laser spot itself, so not all of the light is even incident on the crystal and (b) we observed significant scattering of the laser from the crystal surface.

References

[93] Ashiotis, G. *et al.* The fast azimuthal integration python library: pyFAI. *J. Appl. Crystallogr.* **48**, 510–519 (2015).

[94] Jiang, Z. GIXSGUI : a Matlab toolbox for grazing-incidence x-ray scattering data visualization and reduction, and indexing of buried three-dimensional periodic nanostructured films. *J. Appl. Crystallogr.* **48**, 917–926 (2015).

[95] Hallani, R. K. *et al.* Structural and electronic properties of crystalline, isomerically pure anthradithiophene derivatives. *Adv. Funct. Mater.* **26**, 2341–2348 (2016).

[96] McGhie, A. R., Garito, A. F. & Heeger, A. J. A gradient sublimer for purification and crystal growth of organic donor and acceptor molecules. *J. Cryst. Growth* **22**, 295–297 (1974).

[97] Jurchescu, O. D., Baas, J. & Palstra, T. T. M. Effect of impurities on the mobility of single crystal pentacene. *Appl. Phys. Lett.* **84**, 3061–3063 (2004).

[98] Wilson, M. W. B. *et al.* Temperature-independent singlet exciton fission in tetracene. *J. Am. Chem. Soc.* **135**, 16680–16688 (2013).

Data availability statement

The datasets generated during and/or analysed during the current study are available in the University of Sheffield's ORDA repository (hosted by figshare), `https://doi.org/10.15131/shef.data.12943496`. Source Data for Figs. 1–6 are provided with the paper.

Code availability statement

The code used to perform the kinetic modelling shown in Figures 4 and 6 is available at `https://github.com/davidbossanyi/sfmodelling`. The TRPL data processing was performed using an application available at `https://github.com/fast-spectroscopy-sheffield/iCCD-kinetics`. Additional code used in the data analysis is available from D.G.B. on request.